Agricultural and Forest Meteorology 323 (2022) 109033

Contents lists available at ScienceDirect

Agricultural and Forest Meteorology

journal homepage: www.elsevier.com/locate/agrformet

Potential of UAV-based sun-induced chlorophyll fluorescence to detect water stress in sugar beet

Na Wang [a,*], Jan G.P.W. Clevers [a], Sebastian Wieneke [b], Harm Bartholomeus [a], Lammert Kooistra [a]

[a] Laboratory of Geo-Information Science and Remote Sensing, Wageningen University and Research, P.O. Box 47, 6700 AA Wageningen, the Netherlands
[b] Remote Sensing Center for Earth System Research, University of Leipzig, Leipzig, Germany

ARTICLE INFO

Keywords:
Sun-induced chlorophyll fluorescence
Crop traits
Water stress
Heat stress
Unmanned aerial vehicle

ABSTRACT

Sun-induced chlorophyll fluorescence (SIF) is a direct indicator of plant photosynthetic activities and can potentially indicate plant physiological changes caused by water stress. However, the direct effect of water stress on the physiological SIF responses in crops at the field level still needs further research to clearly understand the involved mechanisms. To study this relationship, we made use of Unmanned Aerial Vehicles (UAVs), which are flexible and cost-effective to acquire SIF data at a high temporal resolution. We acquired near-infrared SIF (760 nm) and red SIF (687 nm) measurements using a UAV platform over irrigated and non-irrigated sugar beet plots. To represent physiological changes in crops, we calculated the apparent SIF yield (SIF normalized by the absorbed photosynthetically active radiation) at 760 and 687 nm ($SIF_{760yield}$ and $SIF_{687yield}$), the fluorescence emission yield at 760 nm (ΦF_{760}), and the SIF_{ratio} (the ratio between SIF_{687} and SIF_{760}). ΦF_{760} was estimated using the recently developed NIRvH approach. For an improved interpretation of the response of these SIF indicators, we also acquired additional UAV-based hyperspectral and thermal data. We found that on June 28, when sugar beets were experiencing water stress, $SIF_{687yield}$, ΦF_{760}, and SIF_{ratio} all showed a significant response to the recovery of the irrigated sugar beets (p-value < 0.05). On the other hand, on July 24 when both water stress and heat stress affected the crop, only ΦF_{760} and SIF_{ratio} weakly tracked the changes induced by the irrigation (p-value < 0.1). ΦF_{760} had similar changes to $SIF_{760yield}$ in both June and July, but ΦF_{760} was more sensitive to irrigation. This indicates the importance of correcting for the structural effect when interpreting the SIF response. The findings suggest that SIF indicators can indicate water stress at the field level, but its value to detect the changes of photosynthetic activities under severe stress needs more investigation.

1. Introduction

Due to changing climate, water shortage for plants (water stress) has been exacerbated by reduced rainfall and changed precipitation patterns (Lobell et al., 2011). Water shortage causes physiological, biochemical, and morphological changes that induce a reduction in photosynthesis. Therefore, water shortage is a critical abiotic stressor limiting crop growth and yield (Lesk et al., 2016). For better management and minimizing harmful effects on crop production, it is critical to detect water stress timely and accurately.

Remote sensing provides spatiotemporal monitoring of crop structural, biochemical, and physiological changes induced by water stress at different scales (Atzberger, 2013). Vegetation indices (VIs) are sensitive to changes in crop canopy structure, leaf pigments, or leaf water content under water stress conditions and may serve as indicators of water stress (Govender et al., 2009; Zarco-Tejada et al., 2013). However, most VIs cannot reveal physiological responses to environmental stressors. This is because they lack a direct connection with photosynthetic functioning. As a result, greenness-based VIs cannot capture short timescale changes (Xu et al., 2021). Therefore, Calderón et al. (2013) suggested that structural and pigment indices were good only to assess damage. Plants can be irreversibly affected before visible symptoms of water stress appear (Jones and Schofield, 2008; Mahajan and Tuteja, 2005). To avoid severe crop damages, a pre-symptomatic or pre-visual detection of plant physiological changes can essentially contribute (Chaerle and Van Der Straeten, 2000). The photochemical reflectance index (PRI) can indicate the short-term changes in xanthophyll pigments under stress conditions (Gamon et al., 1997, 1992), thus it can be a potential pre-visual indicator

* Corresponding author.
E-mail address: na1.wang@wur.nl (N. Wang).

https://doi.org/10.1016/j.agrformet.2022.109033
Received 4 November 2021; Received in revised form 7 April 2022; Accepted 30 May 2022
Available online 6 June 2022

of water stress. However, PRI has been shown to be strongly affected by canopy structure and leaf pigmentation (Gitelson et al., 2017). The initial plant response to water stress is stomatal closure to prevent water loss via transpiration (Chaves et al., 2002; Jones and Schofield, 2008), resulting in an overall increase in plant leaf and canopy temperature compared to a well-watered plant. Thermal remote sensing of leaf and canopy temperature has therefore become an established method to detect pre-visual water stress (Jackson et al., 1981; Maes and Steppe, 2012). However, the major limitation of the temperature-based approach is that the use of leaf or canopy temperature values alone cannot directly estimate the physiological status of plants (Gerhards et al., 2019).

Plant photosynthesis is one of the key physiological phenomena which is strongly affected by water stress (Chaves et al., 2002; Farooq et al., 2009). Annual broadleaf crop photosynthesis is, in particular, sensitive to moisture stress due to leaf stomatal closure, improper photosynthetic machinery, reduced leaf expansion, and decreased leaf pigment concentration, resulting in strong downregulation of photosynthesis (Fu and Huang, 2001; Wahid et al., 2007). However, photosynthesis is a complex physiological process depending on various biophysical parameters and chemical reactions, and it is highly regulated by changing environmental conditions (Farquhar et al., 2001; Schurr et al., 2006; Turner et al., 2001).

Chlorophyll fluorescence (CF) is considered a direct and powerful measurement of the functional status of photosynthesis (Lichtenthaler and Rinderle, 1988). Light energy absorbed by plant chlorophyll has three main dissipating pathways, which consist of photosynthesis (photochemical quenching, PQ), heat dissipation (non-photochemical quenching, NPQ), and fluorescence emission in wavelengths between 650 and 800 nm characterized by two peaks at approximately 685 and 740 nm. Any alteration in the efficiency of one of the pathways can affect the other two (Porcar-Castell et al., 2014). Sun-induced CF (SIF), a continuous emission signal from photosystems II and I, has been intensively studied to further understand vegetation photosynthetic activities on a large scale (Frankenberg and Berry, 2018; Goulas et al., 2017; Guanter et al., 2021; Pérez-Priego et al., 2015; Rascher et al., 2009; Yang et al., 2015). Physiological responses of SIF during stress have been explored at the ground level (e.g. Helm et al., 2020; Marrs et al., 2020; Paul-Limoges et al., 2018; Xu et al., 2018), at the airborne level (e.g. Camino et al., 2018; Gerhards et al., 2018; Panigada et al., 2014; Pinto et al., 2020; Wieneke et al., 2016; Zarco-Tejada et al., 2012), and at the ecosystem scale (e.g. Chen et al., 2021; Lee et al., 2013; Sun et al., 2015; Wang et al., 2019; Yoshida et al., 2015).

Ground-based SIF measurements (e.g. tower-based) cannot assess spatial variation in SIF within the crop field (Wang et al., 2021). Although medium- or high-altitude airborne-based measurements (e.g. HyPlant) can provide valuable spatial information on stress levels over a particular study area, these platforms are costly, and they lack the flexibility of measuring SIF at a high temporal resolution (Bandopadhyay et al., 2020). As an alternative, unmanned aerial vehicles (UAVs) offer cost-efficient ways to monitor crop fields with high spatial and temporal resolution at a low flying altitude (Chang et al., 2020; Bendig et al., 2018, 2021). This low-cost approach also provides an option to bridge the gap between in situ and airborne observations, enhancing stress detection at different spatial scales (Mohammed et al., 2019). Therefore, low-altitude UAV-based SIF can be of great potential for monitoring water stress within crop fields.

However, the response of SIF to water stress is complex and is still not completely understood. The SIF signal is relatively small compared to reflected sunlight (about 1- 5% in the near-infrared region, NIR) and is affected by various factors such as physiological status (Porcar-Castell et al., 2014), canopy structure (Dechant et al., 2020), biochemical constituents (Verrelst et al., 2015), illumination condition (Van der Tol et al., 2016), and sun-target-viewing geometry (Lu et al., 2020; Pinto et al., 2017). In addition, plant response to water stress is expressed by a variety of physiological changes (e.g., stomatal behavior, and leaf water content), biophysical changes (energy balance, leaf, and canopy structure), and photochemical processes (Gerhards et al., 2019). These factors complicate the response of SIF and reduce the predictability of actual crop photosynthetic status under water shortage. As a result, there is no universal relationship between photochemistry and fluorescence emission under stress conditions, meaning that fluorescence can either increase or decrease, depending on the nature of the stressor and the physiological status of the plants (Porcar-Castell et al., 2014; Zeng et al., 2022). In addition, some studies found that SIF at leaf level or proximal level may not indicate the photosynthetic changes caused by water stress (Helm et al., 2020; Marrs et al., 2020), which are discrepant from some satellite SIF observations (Sun et al., 2015). This emphasizes the necessity of further understanding the potential of SIF in water stress detection at the field level.

This study aims to explore the potential of UAV-based SIF indicators to detect water stress within a sugar beet field. An approach using optical reflectance, thermal imagery, and SIF enables us to obtain useful information about the current plant status, and it can also provide a better understanding of how different factors may affect the dynamics of SIF under stress (Calderón et al., 2013; Camino et al., 2018; Gerhards et al., 2018; Panigada et al., 2014; Pinto et al., 2020; Xu et al., 2021, 2018; Zarco-Tejada et al., 2012). We utilized additional remotely sensed signals of the canopy temperature, canopy structure, and leaf pigments to improve the interpretation of the top-of-canopy (TOC) SIF at the wavelength of 687 nm (SIF_{687}) and 760 nm (SIF_{760}) under drought conditions. During the two measurement campaigns, sugar beet plants were affected by drought (June 2019) and by a combination of drought and heat stress (July 2019). A combination of temperature indices, VIs, and soil moisture measurements was used to determine the stress conditions and plant status. We hypothesize that i) SIF indicators can track the plant responses to drought in June and the combined heat and drought stress in July, and ii) SIF indictors react differently under the two different stress conditions.

2. Materials and methodology

2.1. Study area

The dataset used in this study was acquired within a sugar beet field (*Beta vulgaris* L., *Urselina*) during the 2019 growing season (Fig. 1). The study site is located at Unifarm, the agricultural experimental research farm of Wageningen University & Research, the Netherlands. The experiment was located at latitude 51° 59′ 17.64″ N and longitude 5° 39′ 21.17″ E. Soil texture is sandy loam. Sugar beet was sown with 0.5 m between rows and 0.18 m within a row on April 1, 2019 (day of year (DOY): 91) and harvested on November 15, 2019 (DOY 319). Canopy closure was reached on June 15 (DOY 166) at BBCH stage 39 (Meier et al., 1993).

Since water deficits in the middle of the growing period tend to strongly affect sugar beet yield (Steduto et al., 2012), we decided to induce water stress and conduct the field experiment in June and July. Fig. 2a shows precipitation, minimum and maximum air temperature (T_a) in June and July 2019. In June, precipitation occurred only before June 22 and the total precipitation amount in June was 77.8 mm. The peak of the maximum air temperature (T_{max}) occurred on June 25 (34 °C). In July, total precipitation was 31.5 mm. A heat wave occurred from July 23 to 26 with the maximum T_{max} on July 25 (38 °C).

To explore crop response to water stress, two treatments with three repetitions were applied in three blocks. Each block randomly consisted of 2 plots (12 m × 30 m), one treatment with three sprinklers for irrigation treatment and the other treatment without irrigation as the control plot (Fig. 1). To determine the required irrigation timepoint, soil moisture (volumetric water content, vol%) at a depth of 65 mm was measured using an ML3 ThetaProbe Soil Moisture Sensor (Delta-T Devices, UK) and plant status was assessed visually once a week. The averaged soil moisture values were 3.5 vol% and 3.81 vol%,

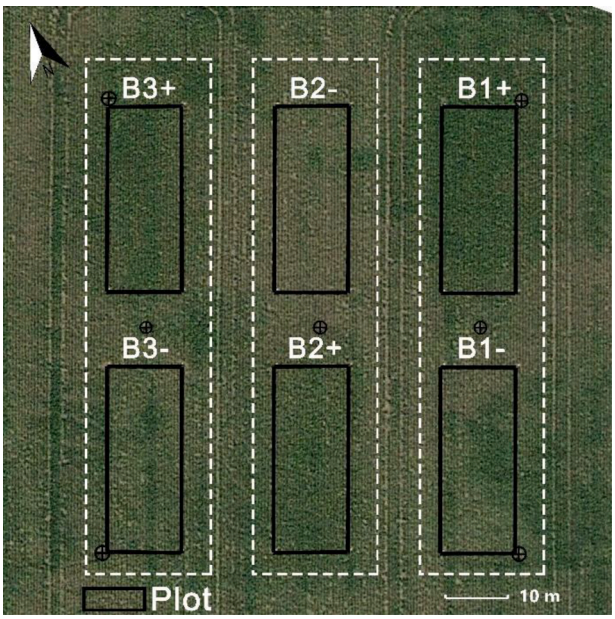

Fig. 1. Location of the plots in the experimental area at Unifarm of Wageningen University, Wageningen, the Netherlands. B1, B2, and B3 refer to block1, block2, and block3 (dotted frames in white) in the sugar beet field. + indicates an irrigation treatment in the plot and – indicates no irrigation treatment (control). The black crosses indicate the ground control points. The base map is a satellite image from Google Earth on July 24, 2019.

respectively, on June 25 and sugar beet leaves visually showed wilting effects. According to two reports on the soil properties in the study field in 2018 from Wageningen Research Unifarm, crops should be irrigated when the soil moisture was below 7.5 vol%. 90 min of irrigation was applied to the irrigation plots on the evening of June 27. Average soil moisture was 2.7 vol% in the irrigation plots and 2.9 vol% in non-irrigation plots on June 27 before irrigation and 16.3 vol% in the irrigation plots on June 28 after irrigation. Leaves showed visual symptoms of water stress (leaf wilting) on July 22. Therefore, we decided to irrigate the sugar beet on the evening of July 23. After the watering, the average soil moisture was 9.5 vol% in the irrigation plots and 2.8 vol% in the non-irrigation plots on July 24. Same management operations were applied to the six plots during the whole growing season except for the two irrigations.

2.2. UAV data acquisition and processing

UAV campaigns were conducted in 2019 on June 27, June 28, July 23, and on July 24 close to solar noon under clear sky conditions. Each flight campaign consisted of 3 flights and lasted about 1 hour on each date. During the flights, the temperature was approximately 21.8 °C and wind speed was 3.6 ~ 4.7 m s^{-1} on June 27, 23.3 °C and 2.4 ~ 3.4 m s^{-1} on June 28, 31.5 °C and 1.7 ~ 2.7 m s^{-1} on July 23, and 36.8 °C and 3.7 ~ 4.7 m s^{-1} on July 24. The solar zenith angle at the beginning of the flight campaign was 30.5° on June 27, 29.3° on June 28, 32.4° on July 23, and 32.5° on July 24.

2.2.1. FluorSpec fluorescence observations

Fluorescence measurements were acquired by the FluorSpec SIF sensor system mounted below a DJI S1000+ UAV platform (DJI, China). The FluorSpec consists of a QE-Pro-spectroradiometer (Ocean Optics Inc., Dunedin, FL, USA), a Global Navigation Satellite System (GNSS) receiver (VarioTek GmbH, Düsseldorf, Germany), a laser rangefinder sensor (LightWare LiDAR LLC, Austin, TX, USA), and a Sony A6000 RGB camera (Sony, Tokyo, Japan). The QE-Pro-is a sub-nanometer spectral resolution point spectrometer, configured with two optical channels to measure the downwelling irradiance and the upwelling radiance in the wavelength range 630–800 nm, with a full-width-at-half-maximum (FWHM) spectral resolution of 0.3 nm and a spectral sampling interval of 0.15 nm. This allows SIF retrieval in the O_2-A absorption band at 760 nm (SIF_{760}) and in the O_2-B absorption band at 687 nm (SIF_{687}). The field-of-view (FOV) of the downward-looking radiance optics is 25° The irradiance channel is equipped with a cosine corrector to collect solar irradiance from a hemispherical FOV (180°). The Sony RGB camera is a standard RGB camera that is automatically triggered together with the spectroradiometer and records high-resolution images of 6000 × 4000 pixels (24 Megapixels). At a flying height of 20 m above ground level (AGL), the camera captures an area of 30 × 20 m with a pixel size of 5 mm. For more details on the FluorSpec system, see (Wang et al., 2021).

FluorSpec flight mission was planned with the universal ground control software (UgCS). The flight mission consisted of three flight lines over the center line of each block and each flight line had five waypoints. Two waypoints were located at the central positions of the short sides of each block and the other three were located at three sprinkler positions. The UAV was programmed to fly 20 m AGL, with a horizontal speed of 1 m s^{-1} from waypoint to waypoint. In this configuration, the spectroradiometer sampled a circular area with a diameter of 8.8 m on the ground for every measurement and the sampling distance was 3.5 m. Each flight lasted around 5 min while the FluorSpec passed over the six sugar beet plots (Fig. 1).

The FluorSpec data processing chain from raw digital numbers (DN) to TOC radiance (Wm^{-2} sr^{-1} nm^{-1}) includes four steps as described in

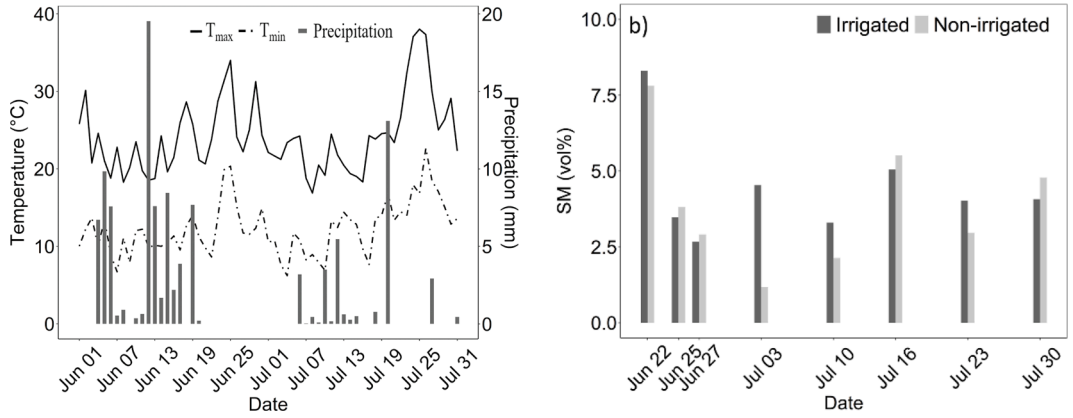

Fig. 2. a) Daily minimum (T_{min}, °C), maximum air temperature (T_{max}, °C), and precipitation (mm) in June and July measured by Weather Station De Veenkampen (2.6 km from the study site), and b) soil moisture (SM, vol%) measured in both irrigation and non-irrigation plots in June and July 2019.

detail in Wang et al. (2021). First, measured raw spectra were converted to at-sensor irradiance and radiance by removing the dark current, dividing by integration time, and multiplying the DN values with the radiometric calibration coefficient per wavelength. Secondly, laser rangefinder and the FluorSpec GNSS data were processed to obtain target-sensor distance and sensor position information, respectively. Next, the at-sensor irradiance and radiance were converted to their TOC equivalents by applying an atmospheric correction using the atmospheric transmittance of the bottom 1 km of atmosphere derived from the MODerate resolution atmospheric TRANsmission (MODTRAN6) algorithm (MODTRAN®, Spectral Sciences, Inc). To get a useful transmittance for a specific UAV altitude, the simulated transmittance can be converted to different thicknesses of the atmosphere using the Beer-Lambert law. Afterward, preceding and following TOC irradiances are linearly interpolated using the GPS timestamp of the corresponding TOC radiance measurement to get TOC irradiance at precisely the same time of the TOC radiance measurement. More details are described in Wang et al. (2021). To improve the geolocation of FluorSpec footprints, the FluorSpec RGB images were manually georectified by matching them with a pseudo-RGB composite using three bands (670 nm, 550 nm, and 514 nm, respectively) of the processed Rikola (preprocessing of Rikoa data refers to Section 2.2.2). Afterwards, the center coordinates of the FluorSpec RGB image determined in the previous step were assigned to the footprint locations of corresponding SIF measurements (Wang et al., under review).

2.2.2. Rikola hyperspectral measurements

Hyperspectral images were acquired on the four measuring dates using a lightweight hyperspectral frame camera (Rikola Ltd., Oulu, Finland) onboard the same DJI S1000+ UAV platform. The camera used is based on a Fabry-Perot interferometer (FPI) (Honkavaara et al., 2013) and was programmatically configured to register 16 narrow spectral bands in a range of 515–870 nm with full width at half maximum (FWHM) varying between 13 and 17 nm (Table S1). These bands were chosen due to their importance to describe changes in biochemical (leaf chlorophyll content) and biophysical (e.g., leaf area index, ground cover, etc.) traits of vegetation at leaf and canopy levels (Clevers and Kooistra, 2011).

The UgCS ground station software was used to plan the flight mission. The study area was captured in 10 flight lines, parallel to the longest side of the area. The flying speed was 2 m s^{-1} and the flight height was 50 m, resulting in a spatial resolution of 25 mm per pixel. The overlap between flight lines was approximately 60%, and within the flight line the overlap between images was approximately 80%. To calibrate the data to reflectance factors, dark current measurements and images of a reflectance reference panel (gray 50% Spectralon panel (LabSphere Inc., North Sutton, NH, USA)) were taken before and after the flight. The flight duration was around 8 min. The HyperspectralImager 2.0 software converted the raw images in digital numbers (registered with 12-bit radiometric resolution) to radiances (Wm^{-2} sr^{-1} nm^{-1}). The radiance images were then transformed into reflectance factor images using the empirical line method (Smith and Milton, 1999; Suomalainen et al., 2014) and the measurement of the Spectralon panel. The images were aligned and ortho- and georectified in Agisoft Metashape Professional (Version 1.5.5) using seven ground control points (GCPs) surveyed with a real-time-kinematic (RTK)-enabled rover, following the data processing protocol described by Roosjen et al. (2017). The georectified Rikola orthomosaic image had a high absolute positional accuracy, with minor deviations of less than ± 2 pixels (25 −50 mm) from the GCP positions.

2.2.3. WIRIS thermal data

Thermal images were acquired by the Workswell WIRIS 640 (Workswell, Prague, Czech Republic) mounted to a gimbal on board an Altura AT8 octocopter (Aerialtronics DV B.V., Katwijk, The Netherlands). The thermal camera has a temperature sensitivity of 0.05 °C and a resolution of 640 × 512 pixels in a spectral range of 7.5–13.5 μm. It captures images recording actual temperature in a TIFF radiometric image format with an emissivity setting of 0.95. The system also is equipped with an RGB camera with a resolution of 1600 × 1200 pixels.

The WIRIS flight pattern consisted of 10 flight lines parallel to the longest side of the blocks. The flight height was 40 m above ground level and the flight speed was 2 m s^{-1}. Images were acquired with a pixel size of 55 × 35 mm. The thermal camera was radiometrically calibrated every 30 min and each flight lasted 7 min.

The calibrated TIFF images were processed and an orthomosaic for the whole trial was constructed with Agisoft Metashape. The georeferencing of the mosaic image was done manually in ArcMap 10.2 using the GCPs measured by RTK. On July 24, the thermal camera did a calibration in the middle of the flight due to a late take-off, resulting in a temperature difference of 6–7 °C in the same area captured before and after the recalibration. It was assumed that the histogram was the same within overlapping areas. Histogram matching (HM) is commonly applied to find a monotonic mapping between a pair of histograms (Gonzalez and Woods, 2006). To solve this mismatch, we applied HM to the overlapping areas of two radiometric images taken exactly before and after the recalibration and used the last image before the calibration as a reference. The returned function was applied to all images taken after the recalibration. The temperature difference in the same area was reduced to less than 0.5 °C. This mismatch was corrected using the histMatch function in R.

2.2.4. Ground measurements

Leaf area index (LAI), chlorophyll concentration (Cab), and soil moisture (SM) observations were collected after the flights on the four measuring dates. On June 27 and July 24, these three types of measurements were measured from six plots, and on June 28 and July 23 ground measurements were acquired only in the three irrigation plots: 8–10 areas of 1 m × 1 m were evenly sampled along the long side of the block. Within each sample site, one LAI measurement was conducted using the LAI-2200C Plant Canopy Analyzer (LI-COR, Lincoln, NE, USA) and five Cab measurements were acquired with a SPAD 502 Plus Chlorophyll Meter (Konica-Minolta, Tokyo, Japan). Each Cab measurement was an average of five random measurements collected from the top leaves of individual plants. SPAD-502 readings were converted to Cab concentrations using the calibration equations in Malnou et al. (2008). SM was conducted at a soil depth of 65 mm with the ML3 ThetaProbe Soil Moisture Sensor.

2.3. Indices applied in water stress detection

2.3.1. Optical vegetation and temperature indices

For optical vegetation indices on canopy structure, we selected the normalized difference vegetation index (NDVI) due to its relationship with the leaf area index (Rouse et al., 1973). The photochemical reflectance index (PRI) has shown promise to remotely estimate dynamics in xanthophyll pigment interconversion at short timesteps and can be used to detect dynamic variations of NPQ (Gamon et al., 1992). Canopy temperature (T_c) has been considered a reliable proxy for plant water status monitoring due to leaf stomatal closure (Jackson et al., 1981). These indices were calculated at pixel level and then averaged at plot level.

2.3.2. SIF indicators

TOC SIF at 760 and 687 nm (SIF_{760} and SIF_{687}) were estimated using the Spectral Shape Assumption Fraunhofer Line Discrimination (SSA-FLD) method (Wang et al., 2021). SSA-FLD is a slightly adapted FLD-based approach to retrieve SIF and can use the ultra-fine spectral information within the oxygen absorption regions. SSA-FLD employs a linear function to describe reflectance and the known shape of a fluorescence spectrum to describe the chlorophyll fluorescence over the

spectral region around the oxygen absorption features (682–689 nm for the O_2-B and 750–780 nm for the O_2-A feature, respectively). For more information, the reader is referred to Wang et al. (2021).

TOC SIF observed above the canopy can be expressed as

$$SIF = PAR \times fAPAR \times \Phi F \times f_{esc} \quad (1)$$

where PAR (W m^{-2}) is the photosynthetically active radiation, fAPAR is the fraction of PAR absorbed by vegetation, ΦF is the physiological fluorescence emission yield of the whole canopy, and f_{esc} is the fraction of all fluorescence photons emitted from all leaves and escaped from the canopy (Guanter et al., 2014).

In this study, TOC SIF at 760 nm and 687 nm normalized by the photosynthetically active radiation absorbed by chlorophyll in green leaves ($SIF_{760yield}$ and $SIF_{687yield}$), the physiological fluorescence emission yield of the whole canopy at 760 nm (ΦF_{760}), and the ratio between SIF_{687} and SIF_{760} (SIF_{ratio}) were applied to indicate the physiological plant response to water stress.

According to Eq. (1), SIF_{yield} can provide insights into canopy scattering and leaf re-absorption and into physiological effects from variations of SIF by accounting for the illumination conditions and the canopy structural and pigment effects on fAPAR (Sun et al., 2015). To calculate SIF_{yield}, PAR was calculated using FluorSpec irradiance measurements acquired before the UAV took off. FluorSpec PAR was firstly calculated within the 630–700 nm interval using 20 consecutive irradiance measurements and then converted to incoming PAR within 400–700 nm using the equation in Wang et al. (2021). The flight duration was 5 min under stable blue-sky illumination conditions. Therefore, PAR measurements before take-off can be applied to normalize SIF and calculate APAR during the flight. We applied a wide dynamic range vegetation index (WDRVI, defined in Eq. (2)) proposed by Gitelson et al. (2005) to calculate fAPAR within FluorSpec footprints (Eq. (3)), which has proved to be linearly correlated with fAPAR (Liu et al., 2019; Viña and Gitelson, 2005).

$$WDRVI = (\alpha \times R_{nir} - R_{red})/(\alpha \times R_{nir} + R_{red}) \quad (2)$$

$$fAPAR = 0.516 \times WDRVI + 0.726 \quad (3)$$

In Eq. (2) R_{nir} and R_{red} are the reflectance at the near-infrared and red band and they were represented by Rikola reflectance at 800 nm and 670 nm, respectively. α is a weighting coefficient with a value of 0.1–0.2 (Gitelson et al., 2014). fAPAR was estimated using the linear regression (Eq. (3)) established by Liu et al. (2019) with α at 0.1. The averaged fAPAR per plot correlated well with LAI ground measurements (Fig. S2), confirming the reliability of the fAPAR estimate.

ΦF is directly linked to the plant physiological changes caused by environmental stress (Porcar-Castell et al., 2014). Far-red ΦF can be calculated as SIF/ (PAR × NIRv) (Dechant et al., 2020; Wang et al., 2020). NIRv is the NIR reflectance of vegetation (Badgley et al., 2017). NIRvH was proposed to calculate the true NIR reflectance of vegetation with minimal soil background impact (Zeng et al., 2021). Therefore, we combined NIRvH and PAR to calculate ΦF at 760 nm for each SIF measurement:

$$\Phi F = SIF/(PAR \times NIRvH) \quad (4)$$

NIRvH can be calculated as

$$NIRvH = R_{nir} - R_{red} - k(\lambda_{nir} - \lambda_{red}) \quad (5)$$

$$k = (R_{nir} - R_{nir1})/(\lambda_{nir} - \lambda_{nir1}) \quad (6)$$

Where R_{nir}, R_{nir1}, and R_{red} are Rikola reflectances at 800 nm, 780 nm, and 680 nm respectively. λ_{nir}, λ_{nir1}, and λ_{red} are the wavelengths of 800 nm, 780 nm, and 680 nm, respectively. As fAPAR was calculated with Rikola reflectances, to be consistent, Rikola reflectances were used to calculate NIRvH. In addition, the time interval between Rikola and FluorSpec flights was approximately 20 min. The solar zenith angle during this interval around solar noon under clear weather conditions would not change significantly. Therefore, the irradiance and sun-sensor geometry were assumed to be comparable for both sensors.

Since SIF_{687} and SIF_{760} have different sensitivity to photosynthetic activities, their ratio (SIF_{ratio}) may be related to physiological changes introduced by a changing contribution of fluorescence emission from Photosystem I (PSI) and Photosystem II (PSII) in response to plant stress (Porcar-Castell et al., 2014; Wieneke et al., 2016;).

2.4. Statistical analysis

To investigate the irrigation effect on the selected indices (Table 1), first, we calculated per plot the difference between the average value of an index on date 1 (before irrigation) and on date 2 (after irrigation) (hereafter called the delta index, Δindex). The null hypothesis (H_0) was that irrigation treatment had no significant effect on the Δindex value as compared to the non-irrigation plots per block, which was tested with a paired *t*-test (Hsu and Lachenbruch, 2014). Spatial heterogeneities might exist between blocks, e.g., due to planting and management history, but by using blocks in an experimental design these are corrected. With a paired *t*-test, the irrigation and non-irrigation plots per block were compared and therefore the block effect was taken into consideration.

3. Results

3.1. Field measurements

Table 2 shows an overview of ground measurements on four experimental dates. On June 27, LAI, Cab, and SM had similar values in irrigation and non-irrigation plots. On June 28, SM in the irrigation plots had increased to 16.24 vol% and LAI had increased from 2.84 to 3.95 cm^2 cm^{-2} (not statistically significant, p-value = 0.22). From July 23 to July 24, for irrigation plots, SM also had a considerable increase from 4.03 to 9.48 vol%, but less than the increase on June 28. The irrigation effect was not noticeable due to a small decrease in LAI (p-value = 0.40). A decrease in Cab was observed both on June 28 and July 24, which was not statistically significant.

3.2. Index maps

To visually evaluate the spatial variation of water stress conditions in the study field, we selected two commonly used indices for water deficit detection, canopy structural parameter NDVI and canopy temperature (T_c) (Fig. 3). Maps of SIF_{760} and SIF_{687} (Fig. 4) show the spatial variability of the signals under drought and drought/heat stress conditions.

Table 1
Parameters of traits evaluated and compared in this study. R represents Rikola reflectance at a specific wavelength. NDVI, PRI, and T_c were averaged per plot using pixel-level values.

Category	VIs	Formula	References
Canopy structure	NDVI	$(R_{800} - R_{670})/(R_{800} + R_{670})$	Rouse et al. (1973)
Xanthophyll pigments	PRI	$(R_{570} - R_{531})/(R_{570} + R_{531})$	Gamon et al. (1992)
Canopy temperature	T_c	T_c	Jackson et al. (1981)
Photosynthesis	$SIF_{760yield}$	$SIF_{760}/(PAR \times fAPAR)$	Papageorgiou. (2004)
	$SIF_{687yield}$	$SIF_{687}/(PAR \times fAPAR)$	Papageorgiou. (2004)
	ΦF_{760}	$SIF_{760}/(PAR \times NIRvH)$	Zeng et al. (2021)
	SIF_{ratio}	$(SIF_{687})/(SIF_{760})$	Agati et al. (1995)

Table 2
Descriptive statistics (mean values ± standard deviations) of leaf area index (LAI, cm^2 cm^{-2}), chlorophyll concentrations (Cab, μg cm^{-2}), and soil moisture (SM, vol%), in irrigation and non-irrigation plots. NA indicates no ground measurements were acquired. + indicates an irrigation treatment applied to the plot and – indicates no irrigation treatment in the plot.

Date	LAI		Cab		SM	
	B+	B–	*B+*	B–	*B+*	B–
June 27	2.84 ±0.87	3.19 ±1.12	52.50 ±6.73	51.71 ±7.23	2.67 ±0.12	2.91 ±1.05
June 28	3.95 ±1.08	NA	46.24 ±6.40	NA	16.24 ±2.01	NA
July 23	2.08 ±0.91	NA	62.83 ±7.42	NA	4.03 ±0.22	NA
July 24	1.86 ±0.45	0.67 ±0.38	48.50 ±13.66	46.58 ±17.58	9.48 ±0.29	2.78 ±0.78

The average values within each plot are shown in Tables S2 and S3. Maps for the other indices are not shown, but in the statistical analysis all indices were included.

3.2.1. NDVI and T_c mapping

Fig. 3 shows spatial patterns of NDVI and T_c measurements within the six plots on the four measuring dates. On June 27 we found higher NDVI values within B1- and B3- and lower values in B2- (Fig. 3a). T_c values in block 1 were lower than in the other two blocks. After irrigation, NDVI showed an increase in the irrigation plots whereas NDVI in non-irrigation plots decreased slightly on the second day (Fig. 3c). Canopy temperature for irrigated areas had a decrease on June 28 and a rise within non-irrigation plots (Fig. 3d).

On July 24 the irrigation did not largely affect NDVI values within irrigation plots, whereas NDVI within non-irrigation plots had a noticeable decrease, particularly within B2– (Fig. 3g). T_c increased within non-irrigated plots and its spatial pattern showed a clear difference in irrigated and non-irrigated plots (Fig. 3h)

3.2.2. Spatial patterns of SIF_{760} and SIF_{687}

The spatial patterns of SIF_{760} and SIF_{687} on the four dates are shown in Fig. 4. In general, SIF_{760} values were higher than SIF_{687} values per plot, particularly on June 27 and June 28. Both metrics showed field heterogeneity which was not easy to be noticed in NDVI and T_c maps. Higher spatial variations can be found in SIF_{760} observations. Clear differences can be noticed within each plot. For example, on June 27 within B2– SIF_{760} varied from 1.68 to 2.42 mW m^{-2} sr^{-1} nm^{-1}, and SIF_{687} ranged within 1.12~1.81 mW m^{-2} sr^{-1} nm^{-1} (Fig. 4a, b). On June 27, SIF_{760} (Fig. 4a) shows a spatial pattern similar to NDVI but opposite to T_c. On June 28, both SIF_{687} and SIF_{760} decreased within all blocks despite the irrigation given to half of the plots (Fig. 4c,d).

On July 23, both values of SIF_{760} and SIF_{687} were lower than those on June 27 (Fig. 4e, f). Averaged SIF_{760} ranged from 0.95 (B2–) to 1.55 mW m^{-2} sr^{-1} nm^{-1} (B1+) and averaged SIF_{687} varied from 0.98 (B2–) to 1.21 mW m^{-2} sr^{-1} nm^{-1} (B3+). After irrigation on July 24, SIF_{760} had obvious decreases in the non-irrigated plots (Fig. 4g). In block1 and 2, SIF_{687} increased more in irrigated plots, while in block3 SIF_{687} decreased for the irrigated B3+ (Fig. 4h).

3.3. Change analysis

Figs. 3 and 4 show the spatial patterns of NDVI, T_c, and SIF and provide a visual evaluation of changes in these indices mainly induced by the imposed irrigation treatment. However, it takes effort to quantify these changes and to better assess the effect of irrigation on these metrics. To compare the response difference between irrigated and non-irrigated plots, we investigated the changes in values of each index acquired on two consecutive experimental days (Δindex).

3.3.1. ΔNDVI, ΔPRI, and ΔT_c

Figs. 5 and 6 present ΔNDVI, ΔPRI, and ΔT_c on two consecutive measuring days in June and July, respectively. As shown in Fig. 5a, after irrigation on June 28, NDVI values increased strongly while they slightly

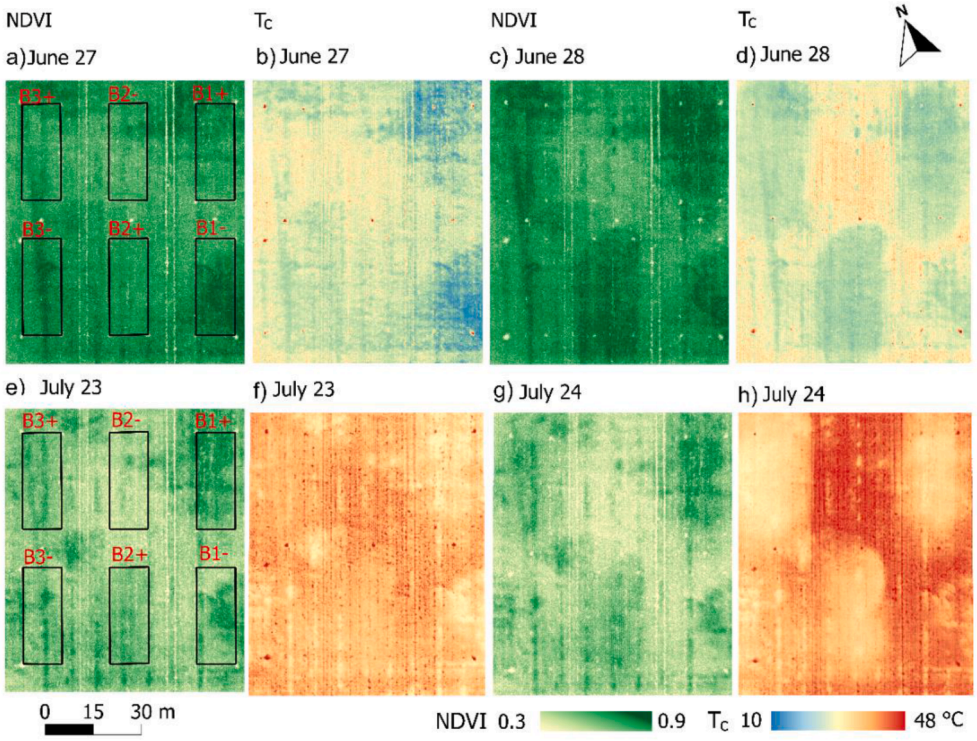

Fig. 3. Maps of NDVI on June 27 (a) and 28 (c), on July 23 (e) and 24 (g). Maps of canopy temperature (T_c) on June 27 (b) and 28 (d), on July 23 (f) and 24 (h). B1, B2, and B3 refer to block1, block2, and block3 in the sugar beet field. + indicates an irrigation treatment applied to the plot and – indicates no irrigation treatment in the plot. Irrigation was given to B1+, B2+, and B3+ on the evenings of June 27 and July 23.

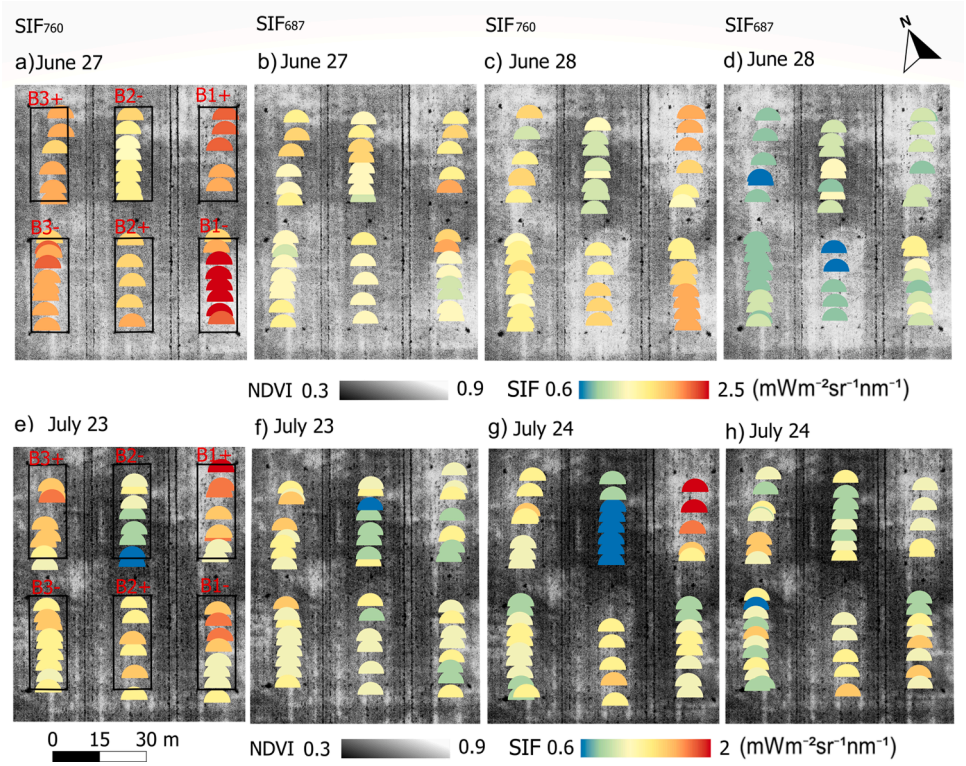

Fig. 4. Maps of SIF_{760} on June 27 (a) and 28 (c), on July 23 (e) and 24 (g). Maps of SIF_{687} on June 27 (b) and 28 (d), on July 23 (f) and 24 (h). B1, B2, and B3 refer to block1, block2, and block3 in the sugar beet field. + indicates an irrigation treatment applied to the plot and – indicates no irrigation treatment in the plot. Irrigation was given to B1+, B2+, and B3+ on the evenings of June 27 and July 23.

decreased in the non-irrigation plots. PRI increased in all plots, but the increase was larger within non-irrigation plots (Fig. 5b). T_c observed from the irrigated canopy decreased and from the non-irrigated canopy increased (Fig. 5c).

On July 24, NDVI declined in all plots (Fig. 6a). Fig. 6b shows that, except for an increase in B1–, PRI showed a small decrease in other plots (Fig. 6b). T_c decreased in B2+ and B3+ and had a substantial increase in B1– and B2–, while in B1+ and B3– it remained almost unchanged before and after the water treatment (Fig. 6c).

3.3.2. *ΔSIF indicators*

To test whether the irrigation effect can also be observed in SIF measurements, the changes for $SIF_{760yield}$, $SIF_{687yield}$, ΦF_{760}, and SIF_{ratio} on the consecutive days are presented in Figs. 7 and 8. On June 28, except for a small increase in $SIF_{687yield}$ within B1–, both $SIF_{760yield}$ and $SIF_{687yield}$ had a reduction in all blocks (Fig. 7a, b). There was no obvious difference in $\Delta SIF_{760yield}$ between the irrigated and non-irrigated plots per block, while this difference in $\Delta SIF_{687yield}$ was much larger. ΦF_{760} reduced in all blocks but less within irrigated plots (Fig. 7c). SIF_{ratio} decreased substantially within irrigation plots and slightly increased within non-irrigation plots except for a small decrease in B3-.

Figs. 8a, b both show an increase in $SIF_{760yield}$ and $SIF_{687yield}$ on July 24. $SIF_{760yield}$ showed a larger increase in irrigated plots in comparison to non-irrigated plots per block. $SIF_{687yield}$ increased slightly less in irrigation plots, making it difficult to differentiate the changes in $\Delta SIF_{687yield}$ in the irrigated plot from the non-irrigated one per block. ΦF_{760} increased more in the irrigated plots than the non-irrigated ones (Fig. 8c). Although SIF_{ratio} increased in all plots, the change was larger in non-irrigated plots (Fig. 8d).

3.4. *Statistical analysis*

Table 3 shows an overview of the effect of irrigation on delta values of NDVI, PRI, and T_c and SIF-based metrics. Both in June and July, NDVI was significantly affected by irrigation treatment, which is in line with the significant changes of NDVI shown in Figs. 3c, g. This finding indicated that the irrigation treatment had a clear effect on the canopy structure of sugar beet plants in our experimental set-up. Irrigation had a significant impact on canopy temperature T_c (Fig. 3d, h) and this impact was greater in June as shown by the higher significance in Table 3. In

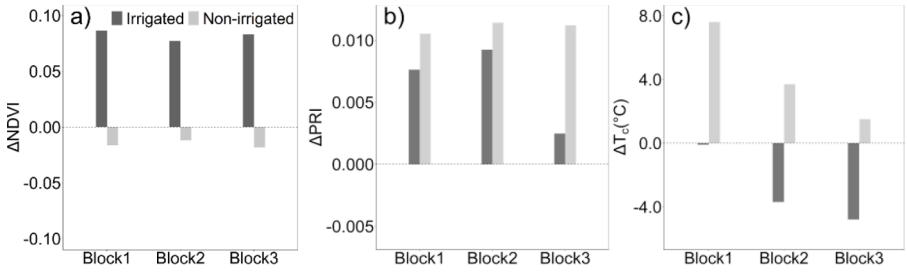

Fig. 5. Delta values (June 28 minus June 27) in NDVI (ΔNDVI) (a), PRI (ΔPRI) (b), and T_c (ΔT_c) (c) in three sugar beet blocks. Irrigated refers to irrigation plots B1+, B2+, and B3+, and non-irrigated refers to non-irrigation plots B1–, B2–, and B3–. Irrigation was given to irrigation plots on the evening of June 27.

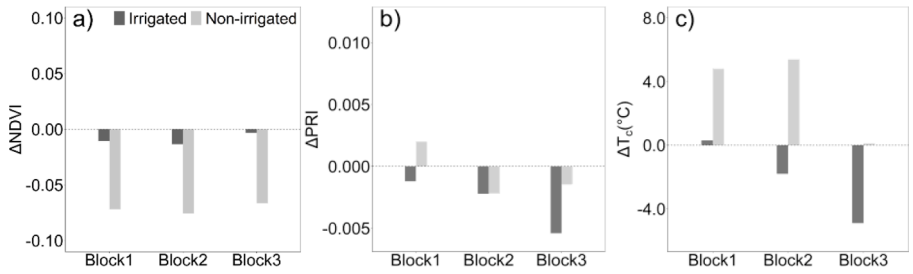

Fig. 6. Delta values (July 24 minus July 23) in NDVI (ΔNDVI) (a), PRI (ΔPRI) (b), and T_c (ΔT_c) (c) in three sugar beet blocks. Irrigated refers to irrigation plots B1+, B2+, and B3+, and non-irrigated refers to non-irrigation plots B1–, B2–, and B3–. Irrigation was given to irrigation plots on the evening of July 23.

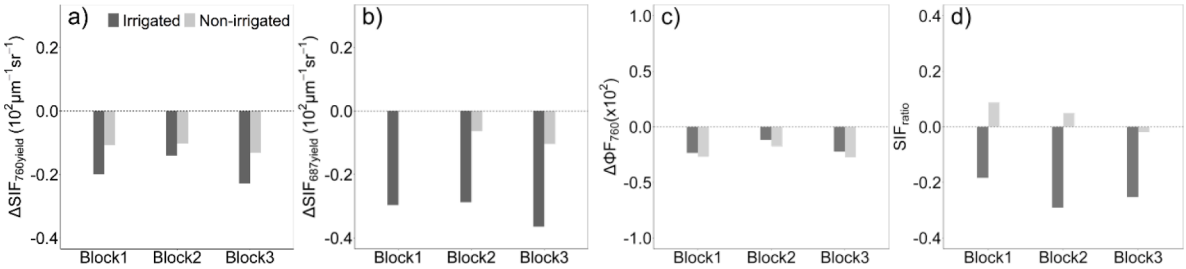

Fig. 7. Delta values (June 28 minus June 27) in $SIF_{760yield}$ ($\Delta SIF_{760yield}$) (a), $SIF_{687yield}$ ($\Delta SIF_{687yield}$) (b), ΦF_{760} ($\Delta \Phi F_{760}$) (c), and SIF_{ratio} (ΔSIF_{ratio}) (d) in three sugar beet blocks. Irrigated refers to irrigation plots B1+, B2+, and B3+, and non-irrigated refers to non-irrigation plots B1–, B2–, and B3–. Irrigation was given to irrigation plots on the evening of June 27.

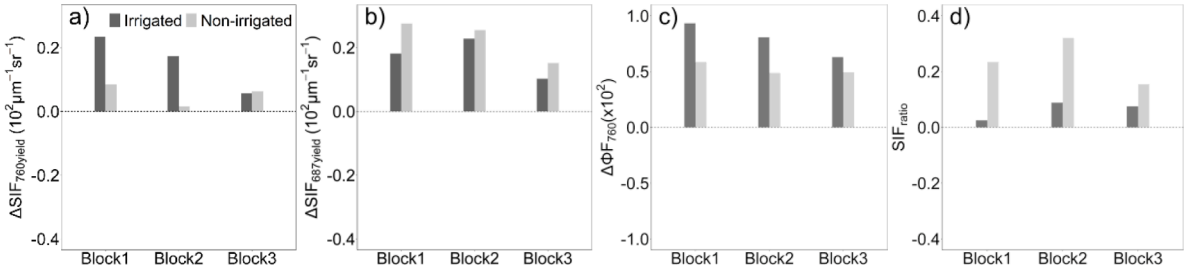

Fig. 8. Delta values (July 24 minus July 23) in $SIF_{760yield}$ ($\Delta SIF_{760yield}$) (a), $SIF_{687yield}$ ($\Delta SIF_{687yield}$) (b), ΦF_{760} ($\Delta \Phi F_{760}$) (c), and SIF_{ratio} (ΔSIF_{ratio}) (d) in three sugar beet blocks. Irrigated refers to irrigation plots B1+, B2+, and B3+, and non-irrigated refers to non-irrigation plots B1–, B2–, and B3–. Irrigation was given to irrigation plots on the evening of July 23.

Table 3
Irrigation effects on different metrics for water stress detection (numbers are statistical significance, ***$p < 0.001$, **$p < 0.01$, *$p < 0.05$, .<0.1, and ns >0.1). These metrics are explained in detail in Section 2.3.

Indices		June 28-June 27	July 24 -July 23
SIF indicators	$\Delta SIF_{760yield}$	0.0585 .	0.204 ns
	$\Delta SIF_{687yield}$	0.0063**	0.1033 ns
	ΦF_{760}	0.0122 *	0.0557 .
	ΔSIF_{ratio}	0.0121 *	0.0680 .
Vegetation indices	ΔNDVI	0.0019 **	8.12e-05 ***
	ΔPRI	0.1560 ns	0.1860 ns
Temperature	ΔT_c	0.0035 **	0.0215 *

June, irrigation significantly affected SIF-based metrics. The responses of $SIF_{687yield}$, ΦF_{760}, and SIF_{ratio} were more pronounced in comparison to $SIF_{760yield}$. However, in July the irrigation effect was weak on ΦF_{760} and SIF_{ratio}. SIF_{yield} both at 760 nm and 687 nm were hardly influenced by the irrigation treatment.

4. Discussion

The objective of this research was to explore the response of UAV-based SIF indicators to water stress in a sugar beet field. VNIR hyperspectral and thermal data were used to assist the interpretation of the SIF metrics. Our results showed that SIF indicators had a pronounced drought response to the irrigation treatment when plants were under water stress (in June), whereas they had a less significant response to the irrigation under combined water limitation and heat stress (in July).

4.1. Field conditions

Plant responses to water stress are complex (Chaves et al., 2002; Hsiao, 1973; Yardanov et al., 2003) and, under field conditions, these responses appear synergistically or antagonistically and are modified by simultaneous plant stresses. For example, heat stress commonly coincides with water scarcity under field conditions. Generally, water loss under heat stress is larger during daytime, mainly due to an increased rate of transpiration, ultimately impairing certain important physiological processes in plants (Fahad et al., 2017). At optimal temperatures (25 °C) photosynthetic capacity only decreased at leaf relative water contents (RWC) around 60%. However, when the temperature rose above the optimum (e.g. 35 °C), photosynthetic capacity was affected at a higher leaf water status (RWC = 80%) (Chaves et al., 2002). In our study, low soil moisture values before irrigation (Table 2) indicated a water deficit occurring in the sugar beet plants on both June 27 and July

23. Sugar beet performs best in a range of temperatures from 17 to 25 °C (Ober and Rajabi, 2010). The maximum air temperature during the observation period did not exceed 24 °C on June 27 and June 28. Therefore, we may assume that temperature was not a limiting factor. In contrast, the extremely high air temperature on July 23 (31.5 °C) and July 24 (36.8 °C) imposed extra heat stress on top of the existing water stress. Irrigation eased the stress in irrigated plots both on June 28 and July 24, indicated by the increase in SM and LAI (Table 2). The irrigation did not reduce the stress on July 24 as much as that on June 28, indicated by lower SM and NDVI and higher T_c on July 24 (Figs. 3 and S3; Table S2).

4.2. Response of SIF indicators to water stress on June 27 and 28

We found that $SIF_{760yield}$, $SIF_{687yield}$, ΦF_{760}, and SIF_{ratio} showed a significant difference between irrigated and non-irrigated sugar beet plants (Table 3). The decrease in SIF_{yield} and ΦF_{760} in non-irrigated plots agrees with the findings from previous studies (Ač et al., 2015; Gerhards et al., 2018; Xu et al., 2021, 2018; Zarco-Tejada et al., 2012). The meta-analysis study carried out by Ač et al. (2015) suggests that water stress, in general, induces a decline in red and far-red fluorescence signal intensity measured at both leaf and canopy levels. The decline could be explained by the activation of non-photochemical mechanisms and the reduction in APAR. As the first and foremost response of almost all C3 plants to water stress, stressed plant stomata closure occurs to prevent water vapor loss via transpiration under water deficit and this results in a decrease in evaporating cooling and therefore an increase in leaf temperature (Chaves et al., 2002; Jones and Schofield, 2008), evidenced by the higher T_c measured over non-irrigated plants on June 28 (Figs. 3d and 5c). Reduced stomatal conductance limits CO_2 intake and consequently increases the generation of reactive oxygen species (ROS) and also affects the electron transport chain in light-dependent reactions (Flexas et al., 2002). Photorespiration increases to prevent oxidative damage in chloroplasts caused by ROS (Voss et al., 2013). NPQ is also upregulated as the dominant way to thermally dissipate the photon energy absorbed, which cannot be processed in photochemical ways. Both energy dissipation mechanisms result in a decrease in photosynthesis rate and fluorescence emission (Porcar-Castell et al., 2014). PRI is sensitive to changes in the xanthophyll cycle which is the driver of the pH-dependent NPQ which acts as the main protection of photosystem II (Goss and Lepetit, 2015). The increased PRI in non-irrigation plots on June 28 (Fig. 5b) could therefore indicate an increase in NPQ. PRI can be affected by canopy structure under stress, confounding its links to NPQ behavior (Gitelson et al., 2017; Schickling et al., 2016). Therefore, PRI should be carefully interpreted to avoid an ill-conditioned situation while exploring the vegetation's physiological response to water stress. In our case, the weak linear regression between PRI and NDVI (R^2 = 0.14) indicated a weak structural effect on PRI, whereas the strong linear correlation in July (R^2 = 0.71) suggested a non-negligible structural effect on PRI. Therefore, PRI could be considered an indicator of NPQ in June, but it might be less informative on in July. In addition, sugar beet leaves rolled and wilted to reduce water loss, resulting in a decrease in effective LAI, which was indicated by the decreased NDVI and fAPAR (Figs. 5a and S2b). As the shortwave radiation on June 27 and 28 were similar (around 798.85 W m^{-2}), APAR in non-irrigation plots decreased and thus could contribute to the decline in SIF emission.

SIF_{yield} and ΦF_{760} also decreased in irrigation plots on June 28. One possible reason could be the regulation of NPQ. Stronger NPQ was triggered to cope with the higher temperature on June 28, indicated by the increase in PRI within irrigated plots, and this resulted in lower fluorescence emission. Irrigated sugar beet plants might physiologically partly or even fully recover from the water stress, as suggested by the decreased T_c (Fig. 5c). Therefore, the quantum yield of PSII increased and fluorescence emission efficiency decreased. Compared to the non-irrigated plants, $SIF_{760yield}$ observed from irrigated plants decreased more, whereas ΦF_{760} decreased less, suggesting a structural effect on SIF_{yield} via the fluorescence escape ratio (f_{esc}) at 760 nm. Some vegetation indices have been proposed to estimate f_{esc} at 760 nm, e.g. the fluorescence correction vegetation index (FCVI) (Yang et al., 2019), the near-infrared reflectance of vegetation (NIRv) (Zeng et al., 2019), and an improved NIRv index (NIRvH) (Zeng et al., 2021). Since FluorSpec and Rikola data do not fully cover the range from 400 to 700 nm needed to calculate FCVI, we calculated NIRvH to estimate f_{esc}. The NIRvH was developed to reduce the sensitivity to the soil background, which was of an additional importance for this study. We found that f_{esc} decreased within the irrigated plots and increased in the non-irrigated ones (Fig. S4a), which could explain why $SIF_{760yield}$ had a larger decrease than ΦF_{760} in irrigated plots. SIF_{ratio} can significantly distinguish the irrigated from the non-irrigated sugar beet plants. The results do not allow us to exclude the possibility that the significant change in the SIF_{ratio} was due to the structural effect of water stress on the re-absorption of SIF_{687} and the scattering of SIF_{760}. Nevertheless, this signal might be a potential indicator of sugar beet actual physiological status, as this ratio varies in response to the changes in the photosynthetic activity of the two photosystems (Agati et al., 1995; Wieneke et al., 2018; Yang et al., 2019).

4.3. Response of SIF indicators to combined water and heat stress on July 23 and 24

Different from findings on June 28, on July 24 we observed an increase in SIF_{yield} at both 687 nm and 760 nm and ΦF_{760} over both irrigated and non-irrigated sugar beet canopies. The response of SIF and ΦF to water scarcity is complex and remains not fully understood. ΦF can either increase or decrease with increasing stress, depending on the severity of stress, the light intensity, the temperature, and NPQ regulation (Zeng et al., 2022). Some previous studies also observed the increase of ΦF under water stress (Chen et al., 2019; Jonard et al., 2020; Martini et al., 2022; Zeng et al., 2022). Electron and light energy are excessive under severe drought. As a result, both NPQ and fluorescence quenching are utilized to consume the absorbed sunlight (Chen et al., 2019). Additionally, PSII is very responsive to temperature and its activity is greatly influenced and even partially terminated under high-temperature stress (Camejo et al., 2006). In this case, NPQ reaches its peak, resulting in a change in the allocation of energy dissipation pathways towards SIF and an increase in the fluorescence emission (Martini et al., 2022; Zeng et al., 2022). The response of SIF_{yield} is co-affected by ΦF_{760} and f_{esc}. f_{esc} decreased within both irrigated and non-irrigated plots (Fig. S4b), implying that the increase of SIF_{yield} was most likely caused by ΦF_{760}.

Only ΦF_{760} and SIF_{ratio} were linked to the changes induced by the irrigation treatment when sugar beet plants were stressed by the water scarcity and the extremely high temperature. The stressed sugar beets had sparse canopies due to leaf wilting or leaf drooping (Table 2, Fig. S3e-h). The strong soil signals within the footprints could affect TOC SIF retrieval (Camino et al., 2018; Wang et al., 2021; Zarco-Tejada et al., 2013) and ΦF estimate (Zeng et al., 2022), increasing the difficulty of detecting the subtle alterations of SIF and SIF indicators. In this case, the value of SIF as an estimator of photosynthesis may decrease. The irrigated sugar beet plants might not fully recover from the combined stress, indicated by the reduced NDVI (Fig. 6a). Consequently, we were not able to observe significant differences in the changes in SIF metrics between the irrigated and non-irrigated plants. ΦF_{760} was more sensitive to the irrigation than $SIF_{760yield}$ (Table 3), likely because ΦF provides insights into physiological stress effects that are decoupled from structural effects. The July case highlights the value of ΦF on stress detection in practice and the necessity to remove the effect of canopy structure changes from TOC SIF observations. Under severe stress, the down-regulation or the photodamage of the photosystem may decouple fluorescence emission from the light reactions of photosynthesis (Helm et al., 2020; Martini et al., 2022), contributing to the non-significant changes in SIF indicators.

4.4. Implications

There is no universal relationship between photochemistry and fluorescence emission under stress conditions. The physiological SIF information might depend on the imposed environmental stresses and severity levels. To support timely irrigation management, the value of UAV-based SIF in water limitation detection should be fully explored. A controlled field experiment where water availability is limited at different levels can provide insights into to what extent SIF can track the crop physiological response and the photosynthetic adjustments. For a better understanding of the response of top-of-canopy SIF to water limitation, it is suggested to take full advantage of the information provided by remotely measured chlorophyll fluorescence. A full picture of energy partitioning on the ground is needed (Marrs et al., 2020). This includes a need to better characterize energy dissipation dynamics. Leaf measurements of photosynthetic parameters, e.g. gas exchange, the quantum yield of PSII, and NPQ, can provide insights into the mechanism linking fluorescence and photosynthesis under different severity levels of water stress. The measurement uncertainty in UAV observations and spatial variation of SIF due to the heterogeneity in soil properties may influence the observed SIF response to water stress. Therefore, SIF measurements from ground-based systems are also recommended as ground-based SIF can reveal the SIF-photosynthesis relation at the proximal canopy level and further facilitate the interpretation and validation of UAV-based SIF observations. In addition, the characterization of canopy structural effects on SIF observations facilitates the interpretation of SIF signals (Verrelst et al., 2015; Yang and Van der Tol, 2018), particularly in understanding and diagnosing plant responses to stress. Canopy structural parameters (e.g. LAI, clumping index, and leaf inclination) affect the absorption of PAR and the SIF escape fraction (f_{esc}) from the canopy (Van der Tol et al., 2019). LAI affects the production of fluorescence and the leaf inclination has a strong effect on the observed fluorescence via f_{esc} (Dechant et al., 2020). For example, planophile leaf orientations of the non-irrigated sugar beet have higher fluorescence than erectophile ones of the well-watered plants (Dechant et al., 2020; Van der Tol et al., 2019; Zeng et al., 2019). In our work, the FCVI- or NIRvH-based approach allowed a rapid decoupling of the canopy structural and functional regulation of far-red TOC SIF. However, these approaches are derived by radiative transfer modeling with a number of assumptions and simplifications or by semi-empirical approaches (Liu et al., 2019; Yang et al., 2020; Zeng et al., 2019). Therefore, they cannot easily disaggregate red SIF into the physiological (ΦF) and structural information due to the within-leaf scattering and re-absorption of red SIF within the leaf or inside a plant canopy (Van der Tol et al., 2019; Yang and van der Tol, 2018). Modeling approaches can describe SIF-relevant processes including absorption, emission, scattering, and re-absorption, e.g. the Soil-Canopy Observation Photosynthesis and Energy fluxes (SCOPE) model (Van der Tol et al., 2009) and the Discrete Anisotropic Radiative Transfer (DART) model (Gastellu-Etchegorry et al., 2017). We suggest using modeling approaches to provide insights into the effects of plant canopy structural, biochemical, and physiological factors on the responses of both red and far-red SIF to water stress (Yang et al., 2019). Furthermore, the analysis of plant properties can benefit greatly from three-dimensional (3D) measurements because plant responses are strongly related to their 3D structure (Omasa et al., 2007). 3D photon and flux tracing RTMs can describe SIF photon interactions with complex 3D canopy structures and support a physical characterization of SIF variability in the field. DART is one of the most comprehensive physically based 3D radiative transfer models and considers the 3D structure (Gastellu-Etchegorry et al., 2017), offering more complex strategies for spatially detailed simulations in structurally complex canopies.

5. Conclusion

The main purpose of this work was to understand the response of UAV-based SIF indicators ($SIF_{760yield}$, $SIF_{687yield}$, ΦF_{760}, and SIF_{ratio}) and to evaluate their potential for water stress detection. Additional remote sensing information such as canopy temperature and vegetation indices including NDVI and PRI were used to characterize the stress status and assist the interpretation of the response of SIF metrics to the irrigation treatment. On June 28, irrigated plants and non-irrigated plants showed significant differences in all indicators. On July 24, the situation was quite different. In addition to water stress, a heatwave also caused severe heat stress. Only ΦF_{760} and SIF_{ratio} could weakly track the changes induced by irrigation in July. ΦF_{760} was more sensitive to irrigation than $SIF_{760yield}$, which underlines the advantage of ΦF_{760} to indicate the physiological changes and the necessity to correct the canopy structural effect on TOC SIF. This study confirms the capacity of SIF acquired by a UAV system to detect stress at the field level. Further investigations are necessary to give a comprehensive understanding of the potential of UAV-based SIF to detect environmental stress at different severity levels and to support crop management in the context of precision agriculture.

Authorship contribution statement

Na Wang conceived the study, designed the experiment, collected UAV-based data and ground measurements, designed and carried out the analysis, and wrote the original draft of the paper. Jan G.P.W. Clevers conceived the study, designed the field experiment, advised on data analysis and visualization of results, and commented on the manuscript. Sebastian Wieneke advised on data analysis and visualization of results and commented on the manuscript. Harm Bartholomeus collected UAV-based data, advised on data analysis, and commented on the manuscript. Lammert Kooistra conceived the study, designed the field experiment, collected UAV-based data, advised on data analysis and visualization of results, and commented on the manuscript.

Declaration of Competing Interest

The authors declare that they have no known competing financial interests or personal relationships that could have appeared to influence the work reported in this paper.

Acknowledgments

This work was supported by the China Scholarship Council (CSC) to N. Wang under Grant 201704910780 and by the Action CA17134 SENSECO (Optical synergies for spatiotemporal sensing of scalable ecophysiological traits) funded by COST (European Cooperation in Science and Technology, www.cost.eu). Authors thank Benjamin Brede, Dainius Masiliūnas, Marcello Novani, Peter Roosjen, and Gerjon Schoonderwoerd from Wageningen University and Research for helping with the field campaign.

Supplementary materials

Supplementary material associated with this article can be found, in the online version, at doi:10.1016/j.agrformet.2022.109033.

References

Ač, A., Malenovský, Z., Olejníčková, J., Gallé, A., Rascher, U., Mohammed, G., 2015. Meta-analysis assessing potential of steady-state chlorophyll fluorescence for remote sensing detection of plant water, temperature and nitrogen stress. Remote Sens. Environ. 168, 420–436. https://doi.org/10.1016/j.rse.2015.07.022.

Agati, G., Mazzinghi, P., Fusi, F., Ambrosini, I., 1995. The F685/F730 chlorophyll fluorescence ratio as a tool in plant physiology: response to physiological and environmental factors. J. Plant Physiol. 145, 228–238. https://doi.org/10.1016/S0176-1617(11)81882-1.

Atzberger, C., 2013. Advances in remote sensing of agriculture: context description, existing operational monitoring systems and major information needs. Remote Sens. (Basel) 5, 949–981. https://doi.org/10.3390/rs5020949.

Badgley, G., Field, C., Berry, J., 2017. Canopy near-infrared reflectance and terrestrial photosynthesis. Sci. Adv. 3 (3), e1602244 https://doi.org/10.1126/sciadv.1602244.

Bandopadhyay, S., Rastogi, A., Juszczak, R., 2020. Review of Top-of-Canopy Sun-Induced Fluorescence (SIF) Studies from Ground, UAV, Airborne to Spaceborne Observations. Sensors 20, 1144. https://doi.org/10.3390/s20041144.

Bendig, J., Chang, C., Wang, N., Atherton, J., Malenovský, Z., Rascher, U., 2021. Measuring solar-induced fluorescence from unmanned aircraft systems for operational use in plant phenotyping and precision farming. 2021 IEEE International Geoscience and Remote Sensing Symposium, pp. 1921–1924. https://doi.org/10.1109/IGARSS47720.2021.9555157.

Bendig, J., Gautam, D., Malenovský, Z., Lucieer, A., 2018. Influence of cosine corrector and UAS platform dynamics on airborne spectral irradiance measurements. IGARSS 2018-2018 IEEE International Geoscience and Remote Sensing Symposium, pp. 8822–8825. https://doi.org/10.1109/IGARSS.2018.8518864.

Calderón, R., Navas-Cortés, J.A., Lucena, C., Zarco-Tejada, P.J., 2013. High-resolution airborne hyperspectral and thermal imagery for early detection of Verticillium wilt of olive using fluorescence, temperature and narrow-band spectral indices. Remote Sens. Environ. 139, 231–245. https://doi.org/10.1016/j.rse.2013.07.031.

Camejo, D., Jiménez, A., Alarcón, J.J., Torres, W., Gómez, J.M., Sevilla, F., 2006. Changes in photosynthetic parameters and antioxidant activities following heat-shock treatment in tomato plants. Funct. Plant Biology 33, 177–187. https://doi.org/10.1071/FP05067.

Camino, C., González-Dugo, V., Hernández, P., Sillero, J.C., Zarco-Tejada, P.J., 2018. Improved nitrogen retrievals with airborne-derived fluorescence and plant traits quantified from VNIR-SWIR hyperspectral imagery in the context of precision agriculture. Int. J. Appl. Earth Observat. Geoinform. 70, 105–117. https://doi.org/10.1016/j.jag.2018.04.013.

Chaerle, L., Van Der Straeten, D., 2000. Imaging techniques and the early detection of plant stress. Trends Plant Sci. 5, 495–501. https://doi.org/10.1016/S1360-1385(00)01781-7.

Chang, C.Y., Zhou, R., Kira, O., Marri, S., Skovira, J., Gu, L., Sun, Y., 2020. An Unmanned Aerial System (UAS) for concurrent measurements of solar-induced chlorophyll fluorescence and hyperspectral reflectance toward improving crop monitoring. Agric. For. Meteorol. 294, 108145 https://doi.org/10.1016/j.agrformet.2020.108145.

Chaves, M.M., Pereira, J.S., Maroco, J., Rodrigues, M.L., Ricardo, C.P.P., Osório, M.L., Carvalho, I., Faria, T., Pinheiro, C., 2002. How plants cope with water stress in the field? Photosynthesis and growth. Ann. Bot. 89, 907–916. https://doi.org/10.1093/aob/mcf105.

Chen, S., Huang, Y., Wang, G., 2021. Detecting drought-induced GPP spatiotemporal variabilities with sun-induced chlorophyll fluorescence during the 2009/2010 droughts in China. Ecol. Indic. 121, 107092 https://doi.org/10.1016/j.ecolind.2020.107092.

Chen, X., Mo, X., Hu, S., Liu, S., 2019. Relationship between fluorescence yield and photochemical yield under water stress and intermediate light conditions. J. Exp. Bot. 70 (1), 301–313. https://doi.org/10.1093/jxb/ery341.

Clevers, J.G., Kooistra, L., 2011. Using hyperspectral remote sensing data for retrieving canopy chlorophyll and nitrogen content. IEEE J. Selected Topics Appl. Earth Observ. Remote Sens. 5, 574–583. https://doi.org/10.1109/JSTARS.2011.2176468.

Dechant, B., Ryu, Y., Badgley, G., Zeng, Y., Berry, J.A., Zhang, Y., Goulas, Y., Li, Z., Zhang, Q., Kang, M., 2020. Canopy structure explains the relationship between photosynthesis and sun-induced chlorophyll fluorescence in crops. Remote Sens. Environ. 241, 111733 https://doi.org/10.1016/j.rse.2020.111733.

Fahad, S., Bajwa, A.A., Nazir, U., Anjum, S.A., Farooq, A., Zohaib, A., Sadia, S., Nasim, W., Adkins, S., Saud, S., 2017. Crop production under drought and heat stress: plant responses and management options. Front. Plant Sci. 8, 1147. https://doi.org/10.3389/fpls.2017.01147.

Farooq, M., Wahid, A., Kobayashi, N., Fujita, D., Basra, S., 2009. Plant drought stress: effects, mechanisms and management. Sustain. Agricul. 153–188. https://doi.org/10.1051/agro:2008021.

Farquhar, G.D., Von Caemmerer, S., Berry, J.A., 2001. Models of photosynthesis. Plant Physiol. 125, 42–45. https://doi.org/10.1104/pp.125.1.42.

Frankenberg, C., Berry, J., 2018. Solar induced chlorophyll fluorescence: origins, relation to photosynthesis and retrieval. Comprehen. Remote Sens. 3, 143–162. https://doi.org/10.1016/B978-0-12-409548-9.10632-3.

Flexas, J., Bota, J., Escalona, J.M., Sampol, B., Medrano, H., 2002. Effects of drought on photosynthesis in grapevines under field conditions: an evaluation of stomatal and mesophyll limitations. Funct. Plant Biol. 29, 461–471. https://doi.org/10.1071/PP01119.

Fu, J., Huang, B., 2001. Involvement of antioxidants and lipid peroxidation in the adaptation of two cool-season grasses to localized drought stress. Environ. Exp. Bot. 45, 105–114. https://doi.org/10.1016/S0098-8472(00)00084-8.

Gamon, J., Penuelas, J., Field, C., 1992. A narrow-waveband spectral index that tracks diurnal changes in photosynthetic efficiency. Remote Sens. Environ. 41, 35–44. https://doi.org/10.1016/0034-4257(92)90059-S.

Gamon, J., Serrano, L., Surfus, J., 1997. The photochemical reflectance index: an optical indicator of photosynthetic radiation use efficiency across species, functional types, and nutrient levels. Oecologia 112, 492–501. https://doi.org/10.1007/s004420050337.

Gastellu-Etchegorry, J.P., Lauret, N., Yin, T., Landier, L., Kallel, A., Malenovský, Z., Al-Bitar, A., Aval, J., Benhmida, S., Qi, J., 2017. DART: recent advances in remote sensing data modeling with atmosphere, polarization, and chlorophyll fluorescence. IEEE J Selected Topics Appl. Earth Observ. Remote Sens. 10, 2640–2649. https://doi.org/10.1109/JSTARS.2017.2685528.

Gerhards, M., Schlerf, M., Mallick, K., Udelhoven, T., 2019. Challenges and future perspectives of multi-/Hyperspectral thermal infrared remote sensing for crop water-stress detection: a review. Remote Sens. (Basel) 11, 1240. https://doi.org/10.3390/rs11101240.

Gerhards, M., Schlerf, M., Rascher, U., Udelhoven, T., Juszczak, R., Alberti, G., Miglietta, F., Inoue, Y., 2018. Analysis of airborne optical and thermal imagery for detection of water stress symptoms. Remote Sens. (Basel) 10, 1139. https://doi.org/10.3390/rs10071139.

Gitelson, A.A., Gamon, J.A., Solovchenko, A., 2017. Multiple drivers of seasonal change in PRI: implications for photosynthesis 2. Stand level. Remote Sens. Environ. 190, 198–206. https://doi.org/10.1016/j.rse.2016.12.015.

Gitelson, A.A., Peng, Y., Huemmrich, K.F., 2014. Relationship between fraction of radiation absorbed by photosynthesizing maize and soybean canopies and NDVI from remotely sensed data taken at close range and from MODIS 250 m resolution data. Remote Sens. Environ. 147, 108–120. https://doi.org/10.1016/j.rse.2014.02.014.

Gitelson, A.A., Vina, A., Ciganda, V., Rundquist, D.C., Arkebauer, T.J., 2005. Remote estimation of canopy chlorophyll content in crops. Geophys. Res. Lett. 32, 8. https://doi.org/10.1029/2005GL022688.

Gonzalez, R.C., Woods, R.E., 2006. Digital Image Pro-Cessing, 3rd Edition. Prentice-Hall, Inc., Upper Saddle River, NJ, USA.

Goss, R., Lepetit, B., 2015. Biodiversity of NPQ. J. Plant Physiol. 172, 13–32. https://doi.org/10.1016/j.jplph.2014.03.004.

Goulas, Y., Fournier, A., Daumard, F., Champagne, S., Ounis, A., Marloie, O., Moya, I., 2017. Gross primary production of a wheat canopy relates stronger to far red than to red solar-induced chlorophyll fluorescence. Remote Sens. (Basel) 9, 97. https://doi.org/10.1016/j.rse.2019.111272.

Govender, M., Govender, P., Weiersbye, I., Witkowski, E., Ahmed, F., 2009. Review of commonly used remote sensing and ground-based technologies to measure plant water stress. Water Sa 35. https://doi.org/10.4314/wsa.v35i5.49201.

Guanter, L., Bacour, C., Schneider, A., Aben, I., van Kempen, T.A., Maignan, F., Retscher, C., Köhler, P., Frankenberg, C., Joiner, J., 2021. The TROPOSIF global sun-induced fluorescence dataset from the Sentinel-5P TROPOMI mission. Earth Syst. Sci. Data Discuss. 1–27. https://doi.org/10.5194/essd-13-5423-2021.

Guanter, L., Zhang, Y., Jung, M., Joiner, J., Voigt, M., Berry, J.A., Frankenberg, C., Huete, A.R., Zarco-Tejada, P., Lee, J.E., Moran, M.S., Ponce-Campos, G., Beer, C., Camps-Valls, G., Buchmann, N., Gianelle, D., Klumpp, K., Cescatti, A., Baker, J.M., Griffis, T.J., 2014. Global and time-resolved monitoring of crop photosynthesis with chlorophyll fluorescence. Proceed. National Acad. Sci. 111, E1327–E1333. https://doi.org/10.1073/pnas.1320008111.

Helm, L.T., Shi, H., Lerdau, M.T., Yang, X., 2020. Solar-induced chlorophyll fluorescence and short-term photosynthetic response to drought. Ecol. Appl. 30, e02101. https://doi.org/10.1002/eap.2101.

Honkavaara, E., Saari, H., Kaivosoja, J., Pölönen, I., Hakala, T., Litkey, P., Mäkynen, J., Pesonen, L., 2013. Processing and assessment of spectrometric, stereoscopic imagery collected using a lightweight UAV spectral camera for precision agriculture. Remote Sens. (Basel) 5, 5006–5039. https://doi.org/10.3390/rs5105006.

Hsiao, T.C., 1973. Plant responses to water stress. Annu. Rev. Plant Physiol. 24, 519–570.

Hsu, H., Lachenbruch, P.A., 2014. Paired t-test. Wiley StatsRef: Statistics Reference Online. https://doi.org/10.1002/9781118445112.stat05929.

Jackson, R.D., Idso, S., Reginato, R., Pinter Jr,, P., 1981. Canopy temperature as a crop water stress indicator. Water Resour. Res. 17, 1133–1138. https://doi.org/10.1029/WR017i004p01133.

Jonard, F., De Canniere, S., Brüggemann, N., Gentine, P., Gianotti, D.S., Lobet, G., Miralles, D.G., Montzka, C., Pagán, B.R., Rascher, U., 2020. Value of sun-induced chlorophyll fluorescence for quantifying hydrological states and fluxes: current status and challenges. Agric. For. Meteorol. 291, 108088 https://doi.org/10.1016/j.agrformet.2020.108088.

Jones, H., Schofield, P., 2008. Thermal and other remote sensing of plant stress. General Appl. Plant Physiol. 34, 19–32.

Lee, J.E., Frankenberg, C., Van der Tol, C., Berry, J.A., Guanter, L., Boyce, C.K., Fisher, J. B., Morrow, E., Worden, J.R., Asefi, S., 2013. Forest productivity and water stress in Amazonia: observations from GOSAT chlorophyll fluorescence. Proceedings of the Royal Society B: Biological Sciences 280, 20130171. https://doi.org/10.1098/rspb.2013.0171.

Lesk, C., Rowhani, P., Ramankutty, N., 2016. Influence of extreme weather disasters on global crop production. Nature 529, 84–87. https://doi.org/10.1038/nature16467.

Lichtenthaler, H.K., Rinderle, U., 1988. The role of chlorophyll fluorescence in the detection of stress conditions in plants. CRC Critical Rev. Analytical Chem. 19, S29–S85. https://doi.org/10.1080/15476510.1988.1040146.

Lobell, D.B., Schlenker, W., Costa-Roberts, J., 2011. Climate trends and global crop production since 1980. Science 333, 616–620. https://doi.org/10.1126/science.1204531.

Lu, X., Liu, Z., Zhao, F., Tang, J., 2020. Comparison of total emitted solar-induced chlorophyll fluorescence (SIF) and top-of-canopy (TOC) SIF in estimating photosynthesis. Remote Sens. Environ. 251, 112083 https://doi.org/10.1016/j.rse.2020.112083.

Liu, X., Guanter, L., Liu, L., Damm, A., Malenovský, Z., Rascher, U., Peng, D., Du, S., Gastellu-Etchegorry, J.P., 2019. Downscaling of solar-induced chlorophyll fluorescence from canopy level to photosystem level using a random forest model. Remote Sens. Environ. 231, 110772 https://doi.org/10.1016/j.rse.2018.05.035.

Maes, W., Steppe, K., 2012. Estimating evapotranspiration and drought stress with ground-based thermal remote sensing in agriculture: a review. J. Exp. Bot. 63, 4671–4712. https://doi.org/10.1093/jxb/ers165.

Mahajan, S., Tuteja, N., 2005. Cold, salinity and drought stresses: an overview. Arch. Biochem. Biophys. 444, 139–158. https://doi.org/10.1016/j.abb.2005.10.018.

Malnou, C., Jaggard, K., Sparkes, D., 2008. Nitrogen fertilizer and the efficiency of the sugar beet crop in late summer. European Journal of Agronomy 28, 47–56. https://doi.org/10.1016/j.eja.2007.05.001.

Martini, D., Sakowska, K., Wohlfahrt, G., Pacheco-Labrador, J., Van der Tol, C., Porcar-Castell, A., Magney, T.S., Carrara, A., Colombo, R., El-Madany, T.S., Gonzalez-Cascon, R., 2022. Heatwave breaks down the linearity between sun-induced fluorescence and gross primary production. New phytologist 233 (6), 2415–2428. https://doi.org/10.1111/nph.17920.

Marrs, J., Reblin, J., Logan, B., Allen, D., Reinmann, A., Bombard, D., Tabachnik, D., Hutyra, L., 2020. Solar-induced fluorescence does not track photosynthetic carbon assimilation following induced stomatal closure. Geophys. Res. Lett. 47, e2020GL087956 https://doi.org/10.1029/2020GL087956.

Meier, U., Bachmann, E., Buhtz, H., Hack, H., Klose, R., Märländer, B., Weber, E., 1993. Phenological growth stages of beta beets (Beta vulgaris L. spp.). Nachrichtenbl Deut Pflanzenschutzd 45, 37–41.

Mohammed, G.H., Colombo, R., Middleton, E.M., Rascher, U., Van der Tol, C., Nedbal, L., Goulas, Y., Pérez-Priego, O., Damm, A., Meroni, M., 2019. Remote sensing of solar-induced chlorophyll fluorescence (SIF) in vegetation: 50 years of progress. Remote Sens. Environ. 231, 111177 https://doi.org/10.1016/j.rse.2019.04.030.

Ober, E.S., Rajabi, A., 2010. Abiotic stress in sugar beet. Sugar Tech. 12, 294–298. https://doi.org/10.1007/s12355-010-0035-3.

Omasa, K., Hosoi, F., Konishi, A., 2007. 3D lidar imaging for detecting and understanding plant responses and canopy structure. J. Exp. Bot. 58, 881–898. https://doi.org/10.1093/jxb/erl142.

Panigada, C., Rossini, M., Meroni, M., Cilia, C., Busetto, L., Amaducci, S., Boschetti, M., Cogliati, S., Picchi, V., Pinto, F., 2014. Fluorescence, PRI and canopy temperature for water stress detection in cereal crops. Int. J. Appl. Earth Observ. Geoinform. 30, 167–178. https://doi.org/10.1016/j.jag.2014.02.002.

Papageorgiou, G.C., 2004. Chlorophyll a fluorescence: a bit of basics and history. In: Govindjee, Papageorgiou GC (Ed.), Chlorophyll a fluorescence: a signature of photosynthesis. *Advances in Photosynthesis and Respiration*,, Vol. 19. Springer, Dordrecht, pp. 1–42. https://doi.org/10.1007/978-1-4020-3218-9_1.

Paul-Limoges, E., Damm, A., Hueni, A., Liebisch, F., Eugster, W., Schaepman, M.E., Buchmann, N., 2018. Effect of environmental conditions on sun-induced fluorescence in a mixed forest and a cropland. Remote Sens. Environ. 219, 310–323. https://doi.org/10.1016/j.rse.2018.10.018.

Pérez-Priego, O., Guan, J.H., Rossini, M., Fava, F., Wutzler, T., Moreno, G., Carvalhais, N., Carrara, A., Kolle, O., Julitta, T., 2015. Sun-induced chlorophyll fluorescence and photochemical reflectance index improve remote-sensing gross primary production estimates under varying nutrient availability in a typical Mediterranean savanna ecosystem. Biogeosciences 12, 6351–6367. https://doi.org/10.5194/bg-12-6351-2015.

Pinto, F., Celesti, M., Acebron, K., Alberti, G., Cogliati, S., Colombo, R., Juszczak, R., Matsubara, S., Miglietta, F., Palombo, A., 2020. Dynamics of sun-induced chlorophyll fluorescence and reflectance to detect stress-induced variations in canopy photosynthesis. Plant Cell Environ. 43, 1637–1654. https://doi.org/10.1111/pce.13754.

Pinto, F., Müller-Linow, M., Schickling, A., Cendrero-Mateo, M.P., Ballvora, A., Rascher, U., 2017. Multiangular observation of canopy sun-induced chlorophyll fluorescence by combining imaging spectroscopy and stereoscopy. Remote Sens (Basel) 9, 415. https://doi.org/10.3390/rs9050415.

Porcar-Castell, A., Tyystjärvi, E., Atherton, J., Van der Tol, C., Flexas, J., Pfündel, E.E., Moreno, J., Frankenberg, C., Berry, J.A., 2014. Linking chlorophyll a fluorescence to photosynthesis for remote sensing applications: mechanisms and challenges. J. Exp. Bot. 65, 4065–4095. https://doi.org/10.1093/jxb/eru191.

Rascher, U., Agati, G., Alonso, L., Cecchi, G., Champagne, S., Colombo, R., Damm, A., Daumard, F., De Miguel, E., Fernandez, G., 2009. CEFLES2: the remote sensing component to quantify photosynthetic efficiency from the leaf to the region by measuring sun-induced fluorescence in the oxygen absorption bands. Biogeosciences 6, 1181–1198. https://doi.org/10.5194/bg-6-1181-2009.

Roosjen, P.P., Suomalainen, J.M., Bartholomeus, H.M., Kooistra, L., Clevers, J.G., 2017. Mapping reflectance anisotropy of a potato canopy using aerial images acquired with an unmanned aerial vehicle. Remote Sens. (Basel) 9, 417. https://doi.org/10.3390/rs9050417.

Rouse, J., Haas, R., Schell J., Deering, D., 1973. Monitoring vegetation systems in the great plains with ERTS. *Third ERTS Symposium*, NASA. 1, 309–317.

Schickling, A., Matveeva, M., Damm, A., Schween, J.H., Wahner, A., Graf, A., Crewell, S., Rascher, U., 2016. Combining sun-induced chlorophyll fluorescence and photochemical reflectance index improves diurnal modeling of gross primary productivity. Remote Sens. (Basel) 8, 574. https://doi.org/10.3390/rs8070574.

Schurr, U., Walter, A., Rascher, U., 2006. Functional dynamics of plant growth and photosynthesis–from steady-state to dynamics–from homogeneity to heterogeneity. Plant Cell Environ. 29, 340–352. https://doi.org/10.1111/j.1365-3040.2005.01490.x.

Smith, G., Milton, E., 1999. The use of the empirical line method to calibrate remotely sensed data to reflectance. Int. J. Remote Sens. 20 (13), 2653–2662. https://doi.org/10.1080/014311699211994.

Steduto, P., Hsiao, T.C., Fereres, E., Raes, D., 2012. Crop Yield Response to Water. Food and Agriculture Organization of the United Nations, Rome, p. 1028.

Sun, Y., Fu, R., Dickinson, R., Joiner, J., Frankenberg, C., Gu, L., Xia, Y., Fernando, N., 2015. Drought onset mechanisms revealed by satellite solar-induced chlorophyll fluorescence: insights from two contrasting extreme events. J.Geophys. Res. 120, 2427–2440. https://doi.org/10.1002/2015JG003150.

Suomalainen, J., Anders, N., Iqbal, S., Roerink, G., Franke, J., Wenting, P., Hünniger, D., Bartholomeus, H., Becker, R., Kooistra, L., 2014. A lightweight hyperspectral mapping system and photogrammetric processing chain for unmanned aerial vehicles. Remote Sens. (Basel) 6 (11), 11013–11030. https://doi.org/10.3390/rs61111013.

Turner, N.C., Wright, G.C., Siddique, K., 2001. Adaptation of grain legumes (pulses) to water-limited environments. Advances in Agronomy 193–231. https://doi.org/10.1016/s0065-2113(01)71015-2.

Van der Tol, C., Rossini, M., Cogliati, S., Verhoef, W., Colombo, R., Rascher, U., Mohammed, G., 2016. A model and measurement comparison of diurnal cycles of sun-induced chlorophyll fluorescence of crops. Remote Sens. Environ. 186, 663–677. https://doi.org/10.1016/j.rse.2016.09.021.

Van der Tol, C., Verhoef, W., Timmermans, J., Verhoef, A., Su, Z., 2009. An integrated model of soil-canopy spectral radiances, photosynthesis, fluorescence, temperature and energy balance. Biogeosci. Discus. 6, 3109–3129. https://doi.org/10.5194/bg-6-3109-2009.

Van der Tol, C., Vilfan, N., Dauwe, D., Cendrero-Mateo, M.P., Yang, P., 2019. The scattering and re-absorption of red and near-infrared chlorophyll fluorescence in the models Fluspect and SCOPE. Remote Sens. Environ. 232, 111292 https://doi.org/10.1016/j.rse.2019.111292.

Verrelst, J., Rivera, J.P., Van der Tol, C., Magnani, F., Mohammed, G., Moreno, J., 2015. Global sensitivity analysis of the SCOPE model: what drives simulated canopy-leaving sun-induced fluorescence? Remote Sens. Environ. 166, 8–21. https://doi.org/10.1016/j.rse.2015.06.002.

Viña, A., Gitelson, A.A., 2005. New developments in the remote estimation of the fraction of absorbed photosynthetically active radiation in crops. Geophys. Res. Lett. 32 https://doi.org/10.1029/2005GL023647.

Voss, I., Sunil, B., Scheibe, R., Raghavendra, A., 2013. Emerging concept for the role of photorespiration as an important part of abiotic stress response. Plant Biol. 15, 713–722. https://doi.org/10.1111/j.1438-8677.2012.00710.x.

Wahid, A., Gelani, S., Ashraf, M., Foolad, M.R., 2007. Heat tolerance in plants: an overview. Environ. Exp. Bot. 61, 199–223. https://doi.org/10.1016/j.envexpbot.2007.05.011.

Wang, C., Guan, K., Peng, B., Chen, M., Jiang, C., Zeng, Y., Wu, G., Wang, S., Wu, J., Yang, X., 2020. Satellite footprint data from OCO-2 and TROPOMI reveal significant spatio-temporal and inter-vegetation type variabilities of solar-induced fluorescence yield in the US Midwest. Remote Sens. Environ. 241, 111728 https://doi.org/10.1016/j.rse.2020.111728.

Wang, N., Suomalainen, J., Bartholomeus, H., Kooistra, L., Masiliūnas, D., Clevers, J.G., 2021. Diurnal variation of sun-induced chlorophyll fluorescence of agricultural crops observed from a point-based spectrometer on a UAV. Int. J. Appl. Earth Observat. Geoinform. 96, 102276 https://doi.org/10.1016/j.jag.2020.102276.

Wang, X., Qiu, B., Li, W., Zhang, Q., 2019. Impacts of drought and heatwave on the terrestrial ecosystem in China as revealed by satellite solar-induced chlorophyll fluorescence. Sci. Total Environ. 693, 133627 https://doi.org/10.1016/j.scitotenv.2019.133627.

Wieneke, S., Ahrends, H., Damm, A., Pinto, F., Stadler, A., Rossini, M., Rascher, U., 2016. Airborne based spectroscopy of red and far-red sun-induced chlorophyll fluorescence: implications for improved estimates of gross primary productivity. Remote Sens. Environ. 184, 654–667. https://doi.org/10.1016/j.rse.2016.07.025.

Wieneke, S., Burkart, A., Cendrero-Mateo, M., Julitta, T., Rossini, M., Schickling, A., Schmidt, M., Rascher, U., 2018. Linking photosynthesis and sun-induced fluorescence at sub-daily to seasonal scales. Remote Sens. Environ. 219, 247–258. https://doi.org/10.1016/j.rse.2018.10.019.

Xu, S., Atherton, J., Riikonen, A., Zhang, C., Oivukkamäki, J., MacArthur, A., Honkavaara, E., Hakala, T., Koivumäki, N., Liu, Z., 2021. Structural and photosynthetic dynamics mediate the response of SIF to water stress in a potato crop. Remote Sens. Environ. 263, 112555 https://doi.org/10.1016/j.rse.2021.112555.

Xu, S., Liu, Z., Zhao, L., Zhao, H., Ren, S., 2018. Diurnal Response of Sun-Induced Fluorescence and PRI to Water Stress in Maize Using a Near-Surface Remote Sensing Platform. Remote Sens. (Basel) 10. https://doi.org/10.3390/rs10101510.

Yang, P., van der Tol, C., 2018. Linking canopy scattering of far-red sun-induced chlorophyll fluorescence with reflectance. Remote Sens. Environ. 209, 456–467. https://doi.org/10.1016/j.rse.2018.02.029.

Yang, P., Van der Tol, C., Campbell, P.K., Middleton, E.M., 2020. Fluorescence Correction Vegetation Index (FCVI): a physically based reflectance index to separate physiological and non-physiological information in far-red sun-induced chlorophyll fluorescence. Remote Sens. Environ. 240, 111676 https://doi.org/10.1016/j.rse.2020.111676.

Yang, P., Van der Tol, C., Verhoef, W., Damm, A., Schickling, A., Kraska, T., Muller, O., Rascher, U., 2019. Using reflectance to explain vegetation biochemical and structural effects on sun-induced chlorophyll fluorescence. Remote Sens. Environ. 231, 110996 https://doi.org/10.1016/j.rse.2018.11.039.

Yang, X., Tang, J., Mustard, J.F., Lee, J.E., Rossini, M., Joiner, J., Munger, J.W., Kornfeld, A., Richardson, A.D., 2015. Solar-induced chlorophyll fluorescence that correlates with canopy photosynthesis on diurnal and seasonal scales in a temperate deciduous forest. Geophys. Res. Lett. 42, 2977–2987. https://doi.org/10.1002/2015GL063201.

Yardanov, I., Velikova, V., Tsonev, T., 2003. Plant responses to drought and stress tolerance. Bulgar. J. Plant Physiol. 187–206. https://doi.org/10.1007/978-3-642-32653-0.

Yoshida, Y., Joiner, J., Tucker, C., Berry, J., Lee, J.E., Walker, G., Reichle, R., Koster, R., Lyapustin, A., Wang, Y., 2015. The 2010 Russian drought impact on satellite measurements of solar-induced chlorophyll fluorescence: insights from modeling and comparisons with parameters derived from satellite reflectances. Remote Sens. Environ. 166, 163–177. https://doi.org/10.1016/j.rse.2015.06.008.

Zarco-Tejada, P.J., González-Dugo, V., Berni, J.A.J., 2012. Fluorescence, temperature and narrow-band indices acquired from a UAV platform for water stress detection using a micro-hyperspectral imager and a thermal camera. Remote Sens. Environ. 117, 322–337. https://doi.org/10.1016/j.rse.2011.10.007.

Zarco-Tejada, P.J., Morales, A., Testi, L., Villalobos, F.J., 2013. Spatio-temporal patterns of chlorophyll fluorescence and physiological and structural indices acquired from hyperspectral imagery as compared with carbon fluxes measured with eddy covariance. Remote Sens. Environ. 133, 102–115. https://doi.org/10.1016/j.rse.2013.02.003.

Zeng, Y., Badgley, G., Dechant, B., Ryu, Y., Chen, M., Berry, J.A., 2019. A practical approach for estimating the escape ratio of near-infrared solar-induced chlorophyll fluorescence. Remote Sens. Environ. 232, 111209 https://doi.org/10.1016/j.rse.2019.05.028.

Zeng, Y., Hao, D., Badgley, G., Damm, A., Rascher, U., Ryu, Y., Johnson, J., Krieger, V., Wu, S., Qiu, H., Liu, Y., 2021. Estimating near-infrared reflectance of vegetation from hyperspectral data. Remote Sens. Environ. 267, 112723 https://doi.org/10.1016/j.rse.2021.112723.

Zeng, Y., Chen, M., Hao, D., Damm, A., Badgley, G., Rascher, U., Johnson, J.E., Dechant, B., Siegmann, B., Ryu, Y., Qiu, H., 2022. Combining near-infrared radiance of vegetation and fluorescence spectroscopy to detect effects of abiotic changes and stresses. Remote Sens. Environ. 270, 112856 https://doi.org/10.1016/j.rse.2021.112856.